International Journal of Extreme Manufacturing

Damage evolution and removal behaviors of GaN crystals involved in double-grits grinding

OPEN ACCESS
IOP Publishing | IMMT
International Journal of Extreme Manufacturing
Int. J. Extrem. Manuf. **6** (2024) 025103 (16pp)
https://doi.org/10.1088/2631-7990/ad207f

Damage evolution and removal behaviors of GaN crystals involved in double-grits grinding

Chen Li[1,2], Yuxiu Hu[1,*], Zongze Wei[1], Chongjun Wu[3], Yunfeng Peng[4], Feihu Zhang[1] and Yanquan Geng[1,2,*]

[1] State Key Laboratory of Robotics and System (HIT), Harbin Institute of Technology, Harbin 150001, People's Republic of China
[2] Key Laboratory of Microsystems and Microstructures Manufacturing (HIT), Harbin Institute of Technology, Harbin 150001, People's Republic of China
[3] College of Mechanical Engineering, Donghua University, Shanghai 201620, People's Republic of China
[4] Department of Mechanical and Electrical Engineering, Xiamen University, Xiamen 361005, People's Republic of China

E-mail: 21b308019@stu.hit.edu.cn and gengyanquan@hit.edu.cn

Received 7 December 2023, revised 3 January 2024
Accepted for publication 19 January 2024
Published 2 February 2024

Abstract

Elucidating the complex interactions between the work material and abrasives during grinding of gallium nitride (GaN) single crystals is an active and challenging research area. In this study, molecular dynamics simulations were performed on double-grits interacted grinding of GaN crystals; and the grinding force, coefficient of friction, stress distribution, plastic damage behaviors, and abrasive damage were systematically investigated. The results demonstrated that the interacted distance in both radial and transverse directions achieved better grinding quality than that in only one direction. The grinding force, grinding induced stress, subsurface damage depth, and abrasive wear increase as the transverse interacted distance increases. However, there was no clear correlation between the interaction distance and the number of atoms in the phase transition and dislocation length. Appropriate interacted distances between abrasives can decrease grinding force, coefficient of friction, grinding induced stress, subsurface damage depth, and abrasive wear during the grinding process. The results of grinding tests combined with cross-sectional transmission electron micrographs validated the simulated damage results, i.e. amorphous atoms, high-pressure phase transition, dislocations, stacking faults, and lattice distortions. The results of this study will deepen our understanding of damage accumulation and material removal resulting from coupling between abrasives during grinding and can be used to develop a feasible approach to the wheel design of ordered abrasives.

Keywords: grinding, double-grits, molecular dynamics, damage, material removal, gallium nitride

* Authors to whom any correspondence should be addressed.

2631-7990/24/025103+16$33.00

1. Introduction

The gallium nitride (GaN) single crystal is the semiconductor with the highest application potential for manufacturing chip wafers due to the large bandwidth, high breakdown voltage, high electron mobility, and stable chemical and physical properties under extreme conditions [1–3]. To fabricate thin chip wafers, bulk GaN crystals must be processed using a sequence of machining methods, including wire saw cutting, grinding, lapping, and polishing. Large chip wafers cannot be machined by lapping and are mainly machined by wire saw cutting, self-rotating grinding, and polishing. Self-rotating grinding can achieve the highest material removal and accurately control the surface shape and thickness of wafers. Self-rotating grinding has thus become necessary for backthinning of chip wafers. However, brittle fractures or micro cracks induced during grinding process can severely deteriorate the application accuracy and service life of crystal components [4–6]. Therefore, numerous researchers focused on conducting polishing [7–10] and high-energy beam etching [11, 12] of GaN semiconductors to eliminate the brittle damages of components. Kubota and Iwakiri [7] carried out a tribochemical reaction to polish GaN substrates, producing a smooth surface with a root-mean-square roughness of 0.133 nm. The tribochemical reaction produced an oxide layer on the substrate surface, enabling removal of the work material under low stress. Pan *et al* [8, 9] performed chemical–mechanical polishing (CMP) tests on GaN semiconductors in conjunction with the electro-Fenton process to promote material removal. Zhang *et al* polished GaN wafers using plasma [11] and electrochemical [12] etching. The wafer surface had subnanometer-scale roughness, and materials were removed at the atomic scale. Although plastic surface free of surface and subsurface cracks was achieved using CMP or high-energy beam etching technologies, the low material removal efficiency of polishing and etching has hindered the large-scale industrial production and application of GaN chips [13–16].

The material removal efficiency of grinding is 10^5–10^7 times that of polishing, and plastic removal produces a considerably lower surface roughness and damage depth than brittle removal. Ductile grinding of hard and brittle crystals could effectively improve the surface quality and reduce the subsurface damage depth, thereby reducing the time required for subsequent polishing. Therefore, considerable effort has been expended to achieve ductile grinding of hard and brittle crystals [17–22], to improve the processing efficiency by ensuring the surface integrity of the crystal components. Shamray *et al* [23] investigated the ductile-to-brittle transition behaviors of Si_3N_4 ceramics, and a Si_3N_4 substrate with a ductile surface and subsurface was obtained by controlling the maximum undeformed chip thickness. Yang *et al* [24] investigated the ductile removal phenomenon of 3C-SiC involved in precision grinding process. Electrolytic in-process dressing was found to facilitate the generation of a compressive residual stress, enabling ductile removal of 3C-SiC. Wang *et al* [25] analyzed how the removal mode affected the acoustic emission (AE) and force during grinding of sapphire. The depth of the ductile-to-brittle transition region could be monitored using the AE data and force curves.

Material removal of semiconductors by grinding occurs largely through mechanical action and to a small extent through the tribochemical reaction. Therefore, the ductile grinding mechanism, i.e. the characteristics of ductile deformation and removal of work materials during grinding, needs to be elucidated to optimize process parameters to achieve high-efficiency and high surface integrity machining of hard and brittle materials [26–29]. Tao *et al* [30] carried out scratching tests and transmission electron microscopy (TEM) to elucidate the mechanism of ductile damage in silicon wafers. This mechanism was found to facilitate high-efficiency production of high-efficiency production of large-size silicon wafers. Li *et al* [31] revealed the ductile grinding mechanism of silicon substrates using single-grit scratching tests and smoothed-particle-hydrodynamics simulations, and they concluded that the understanding of ductile mechanism would provide theoretical guidance for optimizing grinding parameters. Wang *et al* [32] used single-grit impact scratching tests to explore the ductile grinding mechanism of β-Ga_2O_3. This mechanism was found to facilitate high-efficiency grinding of brittle materials. Single-grit scratch tests were performed in conjunction with cross-sectional TEM to investigate the plastic deformation of monocrystalline GaN induced during grinding. The main forms of plastic deformation were a high-pressure phase transition, an amorphous transition, stacking faults, dislocations, nanocrystals, and lattice distortions [33–35]. However, as a result of the random distribution of abrasives and complex interactions between the work material and abrasives [36–39], the effect of coupling between randomly located abrasives on damage accumulation and material removal during grinding of GaN single crystals remains unclear.

Ultra-precision grinding experiments cannot quantitatively characterize the influence of coupling actions between abrasive particles on damage accumulation and material removal [40, 41]. High-speed scratching experiments at the nanoscale cannot accurately control the machining depth and measure the high-frequency scratching force exerted by abrasives. Therefore, researchers have performed molecular dynamics (MD) simulations on double- and multiple-grits grinding to investigate grinding-induced damage accumulation and material removal [42–48]. Meng *et al* [42] used MD method to investigate the coupling between abrasives on material removal behavior during double-grits grinding of 6H-SiC crystals. The coupling among multiple abrasives during machining helped improve the surface smoothness and decrease subsurface damages. Guo *et al* [43] performed MD simulations of multiple-grits grinding of monocrystalline silicon, and they found that multiple-grits grinding effectively decreased the thickness of the damage layer induced by the single-grit grinding. Zhou *et al* [44] used MD method to simulate material removal process involved in multi-abrasives machining of SiC substrates. The distribution and exposed height of the abrasives strongly affected the machining temperature and subsurface damage. Zhao *et al* [45] studied how the superposition of abrasives affected the surface generated during double-grit grinding of monocrystalline silicon. The

superposition of abrasives was found to reduce the tangential force and temperature but increase the residual stress. Hu *et al* [46] performed MD simulations to investigate the coupling between double grits during vibration-assisted grinding of single-crystal SiC, and defined an overlap ratio to describe the coupling degree between double grits. The MD results showed that the coupling degree of the abrasives increased with the overlap ratio, substantially improving the machining efficiency and surface integrity. MD simulations can reproduce transient removal characteristics during chip grinding, which is difficult to capture in a grinding experiment, and quantitatively analyze the damage accumulation and material removal behaviors induced by abrasive machining [49–51]. These simulations can elucidate the influence of coupling actions of abrasive particles on the stress distribution [52], phase transition [53], grinding force [54], and coefficient of friction [55] during grinding process, which can provide a beneficial guidance for the optimization of grinding processes. Nevertheless, however, no MD simulations of double-grit grinding of GaN semiconductors have been reported thus far. Therefore, the current understanding of the grinding mechanism for GaN semiconductors remains at the level of single-grit-induced damage and removal [56–59].

In this study, MD simulations were conducted on double-grit grinding of monocrystalline GaN. The interaction distance of the abrasives was correlated with the grinding force, coefficient of friction, stress distribution, subsurface damage, and abrasive damage. A grinding test was performed in conjunction with cross-sectional TEM to verify the simulation accuracy. The results of this study provide insight into damage evolution and removal during grinding of hard and brittle materials and can be used to develop a feasible approach to the wheel design of ordered abrasives.

2. Simulation and experimental conditions

2.1. Simulation conditions

Two kinds of MD models for double-grits interacted grinding of GaN crystals were established using LAMMPS software. Both models consisted of a workpiece with a dimensions of 27.5 nm × 20 nm × 10 nm and two hemispherical abrasives with a radius of 3 nm. Three kinds of atoms were used in both the abrasive and workpiece models, namely, boundary, thermostat, and Newtonian atoms. The atomic positions in the boundary layer were fixed to prevent the workpiece from translating under the action of the grinding force. The coupling constant of the thermostat was selected to be 0.1 ps. The interacted distance of the two abrasives perpendicular to the grinding direction is called the transverse interacted distance, L_a. The interacted distance of the two abrasives along the grinding direction is called the radial interacted distance, L_b. Figure 1(a) shows the first model in which both L_a and L_b (=6 nm) are nonzero. Figure 1(b) shows the second model, in which only L_a is nonzero. All the grinding simulations were performed on the (0001) plane and along the [11–20] direction. The grinding depth, grinding length and speed were set as 2 nm, 17 nm, and 50 m·s^{-1}, respectively. The relaxation and grinding processes of the abrasives and work material were simulated in the NVT and NVE ensembles, respectively. The two abrasives cut the workpiece simultaneously during the simulation.

The Tersoff potential is a three-body potential function that can accurately describe the length, angle, and energy of a bond between atoms, thereby providing a realistic description of covalent bonded materials [60, 61]. The Tersoff potential shown in equation (1) was used to model the interaction between the ions in GaN crystals [62],

$$E_{\mathrm{GaN}} = \sum_{i>j} f_c\left(r_{ij}\right)\left[V_{ij}^{R}\left(r_{ij}\right) - \overline{B_{ij}} V_{ij}^{A}\left(r_{ij}\right)\right] \tag{1}$$

where $f_c(r)$, V_{ij}^{A}, V_{ij}^{R}, and $\overline{B}_{ij}$ denote the cut-off function, attractive energy, repulsive energy, and bond-order parameter, respectively. The values of the key parameters in the Tersoff potential are detailed in [62].

The interaction of C ions in diamond abrasives was described by the LCBOP potential [63] given in equation (2),

$$E_{\mathrm{C}} = \frac{1}{2}\sum_{i,j}^{N} V_{ij}^{\mathrm{tot}} = \frac{1}{2}\sum_{i,j}^{N}\left[f_c\left(r_{ij}\right) V_{ij}^{\mathrm{SR}} + \left(1 - f_c\left(r_{ij}\right)\right) V_{ij}^{\mathrm{LR}}\right] \tag{2}$$

where V_{ij}^{tot}, V^{SR}, and V^{LR} denote the total pair interaction, short-range section, and long-range section, respectively. The values of the key parameters in the LCBOP potential are detailed in [63].

In addition, the C–N and C–Ga interactions were described by the 12/6 Lenard–Jones potential [34] given in equation (3),

$$E = 4\varepsilon\left[\left(\frac{\sigma}{r}\right)^{12} - \left(\frac{\sigma}{r}\right)^{6}\right], r < r_c \tag{3}$$

where ε denotes the attractive well depth, r_c denotes the cut-off radius whose value is 0.25 nm, and σ denotes the interparticle distance.

To investigate the influence of the interacted distance on material deformation and removal characteristics, simulations were carried out on interactive double-grit grinding with different interaction distances according to the scheme presented in table 1. Given the computational difficulty of running MD simulations with the dimensions of an actual grinding process, we reduced both the size and spacing of the abrasives by the same multiple. For $L_b = 0$, a minimum L_b of 6 nm was needed to prevent interference between the two abrasives. In addition, a simulation on single-grit grinding was performed as a control. During the simulation, the additional kinetic energy generated by the movement of atoms along the grinding direction was removed to ensure the accuracy of the simulation results. The simulation results were analyzed using OVITO visualization software.

2.2. Experimental conditions

To validate the simulated results, an grinding experiment was performed on monocrystalline GaN using a ultraprecision self-rotating grinder, as shown in figure 2. The GaN specimen was 10.5 mm long, 10 mm wide, and 0.35 mm thick. To

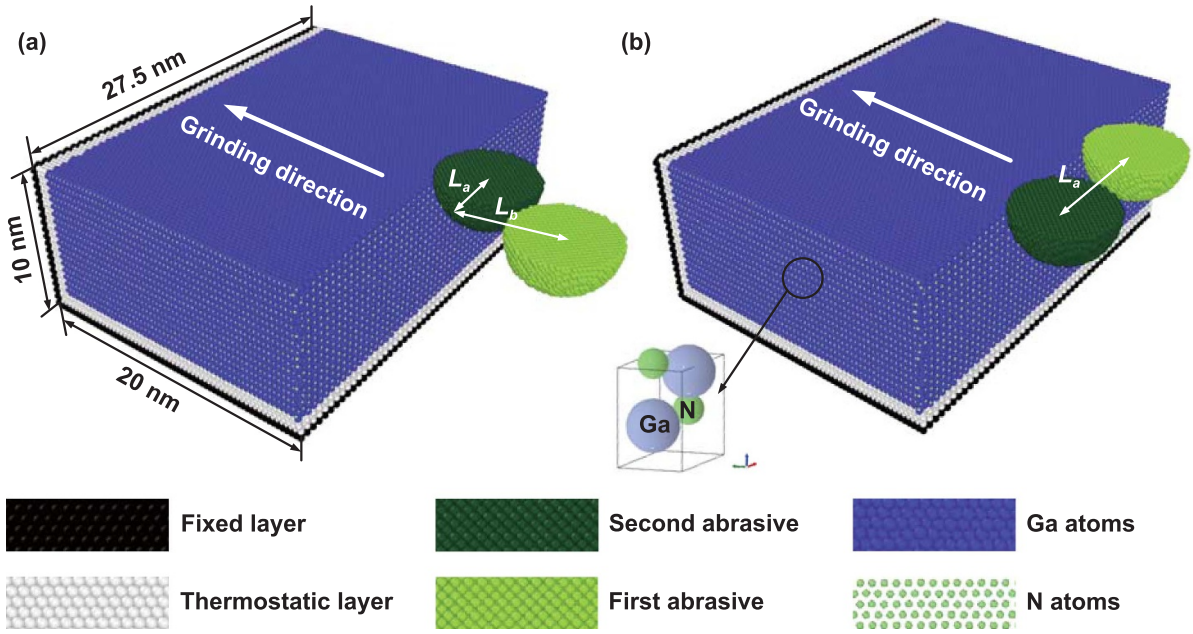

Figure 1. Molecular dynamics (MD) model of double-grits interacted grinding of monocrystalline GaN for a radial interacted distance L_b of (a) 6 nm and (b) 0 nm.

Table 1. Detailed scheme of double-grits interacted grinding simulations.

Group No.	Transverse interacted distance L_a (nm)	Radial interacted distance L_b (nm)	Abrasive number
1	0	0	1
2–8	1–7	6	2
9–17	6–10	0	3

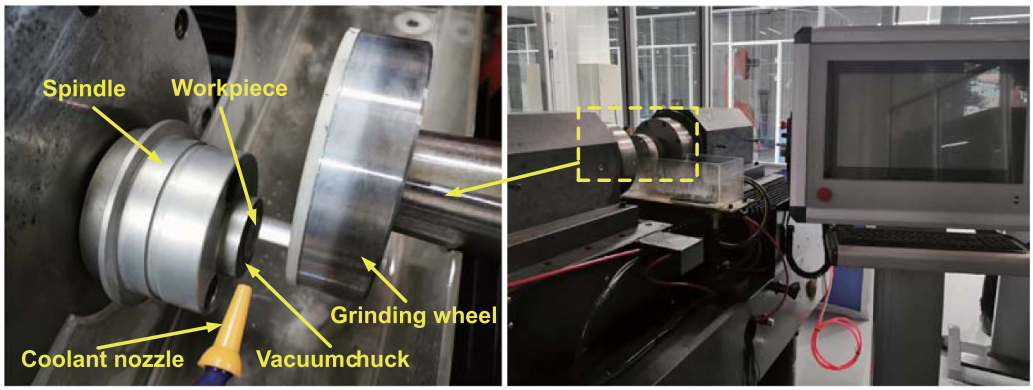

Figure 2. Self-rotating grinding platform used to perform experiments on GaN crystals.

ensure that the GaN specimen was not damaged during preparation for the grinding test, CMP was performed on the specimen to achieve a surface roughness below 2.0 nm in Ra. Ceramic bonded diamond grinding wheels with mesh size of #8000 and diamater of 125 mm were used in the grinding experiment. The rotational speeds of the wheel and workpiece were 1500 and 100 r·min^{-1}, respectively. The feed rate was 12 μm·min^{-1}. Oil coolants were used in grinding process to decrease the grinding temperature and wheel wear. After the grinding test, an TEM sample of the ground subsurface was prepared by using a focused ion beam, and the subsurface damage was analyzed by the cross-sectional TEM method. The accelerating voltage, TEM linear resolution, high-resolution TEM (HR-TEM), TEM magnification, and scanning transmission electron microscopy (STEM) magnification of the TEM (Talos F200x, USA) are 200 kV, 0.14 nm, 0.1 nm, 25–1500 000, and 150–2300 000, respectively.

Equation (4) [21] was used to calculate the uncut chip thickness d_g under the grinding conditions used in this study as 0–17.8 nm:

$$d_g = 2.44R_g\left(\frac{f_s r n_w}{\pi d_s b_s \gamma n_s^2}\right)^{0.4} \tag{4}$$

where d_g is the uncut chip thickness, R_g is the abrasive radius, f_s is the feed speed, r is the distance from the workpiece center, n_w is the rotational speed of the work material, d_s is the outer diameter of the wheel, b_s is the width of the wheel, γ is the volume content of the abrasives, and n_s is the wheel rotational speed.

3. Results and discussions

3.1. Grinding force and coefficient of friction

Grinding force is an important index for evaluating the machining effect during the grinding process, and indirectly reflects the material removal process and interaction between the abrasives and workpiece. Figure 3 shows the grinding forces under different interacted conditions. Both figures 3(a) and (b) indicate that as the grinding length increases, the grinding force increases and then stabilizes. Therefore, the average grinding force at the stable grinding stage can be used to analyze the influence of the interacted distance on the grinding force. Figure 3(a) also shows that the grinding force is smaller for the second abrasive than the first abrasive because of the elimination of coupling actions between the two abrasives. Figure 3(c) shows that for $L_b = 6$ nm and increasing L_a, the grinding force increases and then stabilizes. This result is obtained because increasing L_a weakens the coupling between the two abrasives, increasing the contact area between the workpiece and abrasives. Figure 3(d) shows that for non-interfering abrasives, there is a specific L_a at which there is no discernible coupling between the abrasives and the grinding force is approximately twice that of a single grit, that is, L_a has no discernible effect on the grinding force.

Figure 4 shows the influence of the transverse interacted distance on the coefficient of friction during double-grits grinding of GaN crystals. In this study, the coefficient of friction is defined as the ratio of the tangential force exerted by the abrasive along the grinding direction to the normal force exerted by the abrasive. In figure 4(a), for $L_b = 6$ nm and increasing L_a, the coefficient of friction decreases and then increases. The atomic displacements shown in the inset images indicate for L_a below 3 nm, the contact area between the workpiece and abrasives increases with L_a. However, there is no discernible increase in the number of atoms that have accumulated in front of the abrasives because of the elimination of coupling between abrasives, which results in the gradual decrease of the coefficient of friction. For L_a above 3 nm, as L_a increases, the effect of eliminating the coupling between abrasives weakens and the number of atoms that have accumulated in front of the abrasives increases, resulting in the gradual increase of the coefficient of friction. Figure 4(b) shows that for $L_b = 0$ nm, L_a has no discernible effect on the coefficient of friction. Selecting appropriate interacted distances can effectively reduce the friction between the workpiece and abrasives below that of single-grit grinding while ensuring efficient material removal, providing a feasible approach to the wheel design of ordered abrasives.

3.2. Stress distribution

The stress investigated in this study corresponds to the von Mises stress, which was calculated by the spatial average method. Figure 5 presents the stress distributions for different transverse interacted distances when the radial interacted distance is 6 nm. The average stress induced by the second abrasive during double-grit grinding (∼49.5–57.5 GPa) is smaller than that induced during single-grit grinding (∼58.1 GPa) because of the elimination of the coupling to the first abrasive. When the transverse interacted distance is 1 nm, the average stress induced by the second abrasive is 14.8% lower than the average stress induced during single-grit grinding. As the transverse interacted distance increases, the coupling removal of the first abrasive weakens, causing the stress induced by the second abrasive to gradually increase and approach that induced during single-grit grinding.

Figure 6 presents the stress distributions under different transverse interacted distances when the radial interacted distance is 0 nm. When the transverse interacted distance is 6 nm, large stresses in the workpiece are mainly concentrated between the two abrasives as well as below the abrasives because of the pushing action of these abrasives. As the transverse interacted distance increases, the coupling effect between the abrasives gradually weakens. Therefore, the stress on the subsurface gradually decreases, and the large stress is gradually transferred to the region below the two abrasives. In addition, the number of chips accumulated between the two abrasives gradually increases with the transverse interacted distance. A very low stress is exerted on the chips because the abrasives no longer push on the material after the chips form.

3.3. Subsurface damage

It is crucial that MD simulations accurately predict material damage phenomena. Therefore, it is particularly important to determine the subsurface damage mechanism of GaN crystals during interactive double-grit grinding. The machining scale in an MD simulation is considerably smaller than the depth of the brittle-to-ductile transition region in GaN crystals. Thus, the simulated subsurface damage is plastic damage, as shown in figure 7. The simulated results demonstrate that the plastic damage of GaN crystals induced by double-grits grinding is dominated by the amorphous transition, high-pressure phase transition, dislocations, stacking faults, and lattice distortions. The atoms in the chips and groove surfaces have high energy and weak structural stability and are therefore most prone to amorphization [64, 65]. The results of Zhang *et al* [66]

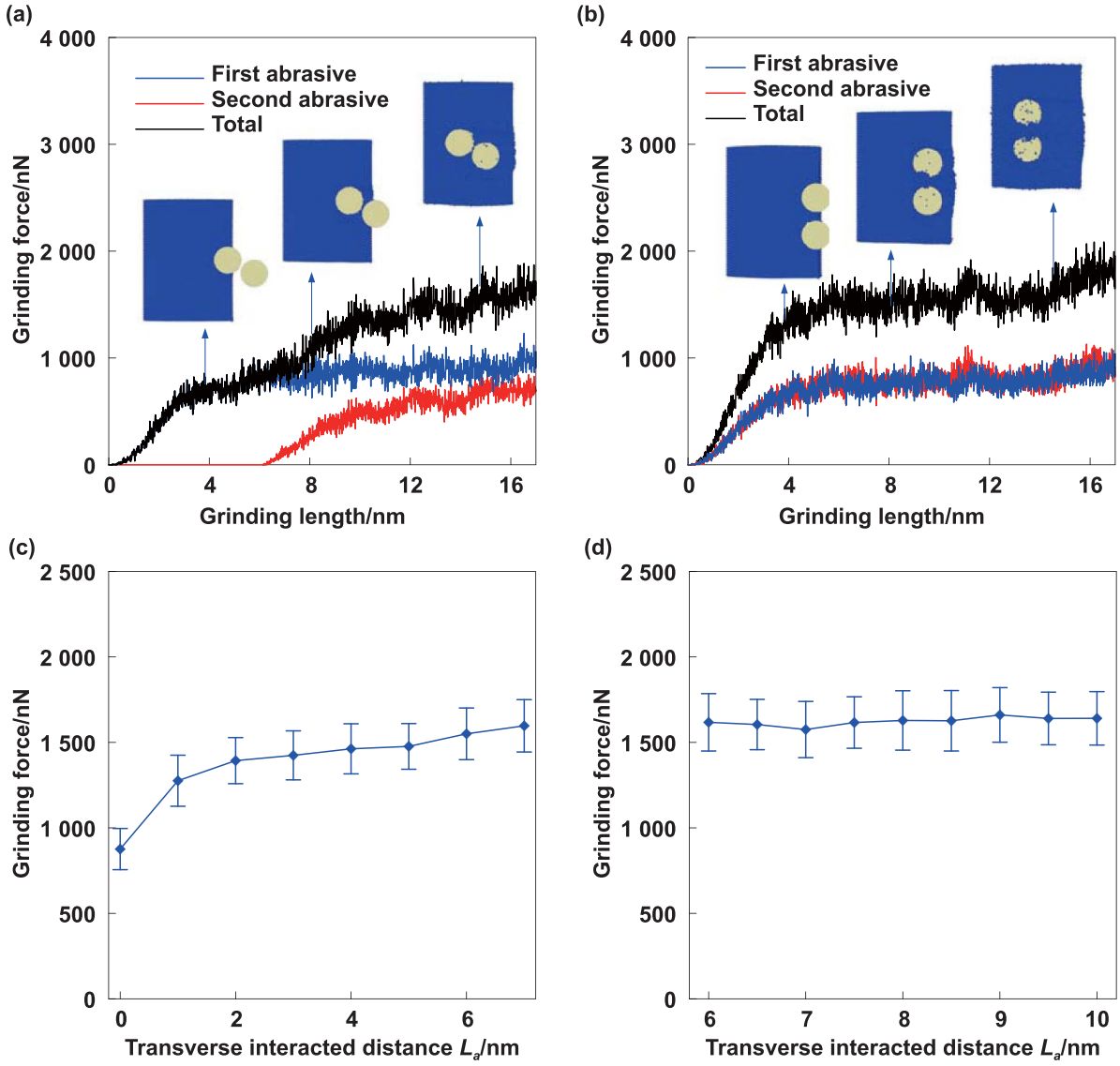

Figure 3. Grinding force for different interacted distances. (a) Grinding force versus the grinding length for radial and transverse interacted distances of 6 nm and 3 nm, respectively. (b) Grinding force versus the grinding length for radial and transverse interacted distances of 0 nm and 8 nm, respectively. (c) Grinding force versus the transverse interacted distance for a radial interacted distance of 6 nm. (d) Grinding force versus the transverse interacted distance for a radial interacted distance of 0 nm.

and Jiang *et al* [67] lead to the conclusion that the maximum stress induced by machining does not occur at the ground surface underneath the abrasive but at a certain distance from the ground surface in the plastic zone. Therefore, the high-pressure phase transition zone lies below the amorphous layer. The plastic zone is surrounded by a large number of stacking faults and dislocations because of the effect of subsurface stress at the boundary of the plastic zone [68, 69]. To eliminate the interference of elastic deformation on the identification of lattice distortion, we selected an area far away from the abrasive after elastic recovery to identify the lattice distortion. Therefore, the results presented in figure 7(h) were confirmed to be lattice distortion rather than elastic deformation. Figure 7(i) shows the phase transition path from hexagonal GaN to cubic GaN that occurs during the grinding process. It can be observed that the high pressure caused by the abrasive destroys the atomic arrangement and lattice structure. The high pressure induced by the abrasive destroys the atomic arrangement and lattice structure. The barrier to the phase transition is overcome by the generation of unstable intermediate phases between the hexagonal and cubic structures. As the pressure increases, the content of hexagonal GaN gradually decreases and the content of cubic GaN gradually increases and then stabilizes. An experiment was performed to confirm the simulation results.

An experiment was performed to characterize the ground subsurface to validate the MD simulation results of the effect of coupling between abrasives on material damage and

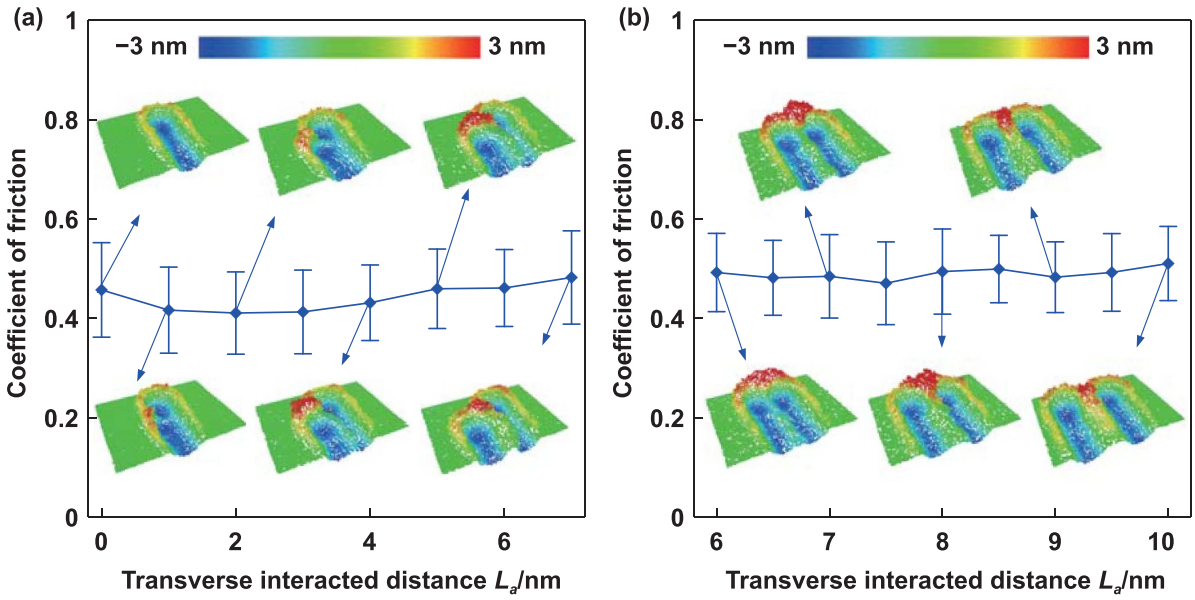

Figure 4. Coefficient of friction under different interacted distances. (a) Coefficient of friction versus the transverse interacted distance for a radial interacted distance of 6 nm. (b) Coefficient of friction versus the transverse interacted distance for a radial interacted distance of 0 nm. The atomic displacements at different interacted distances are shown in the inset images.

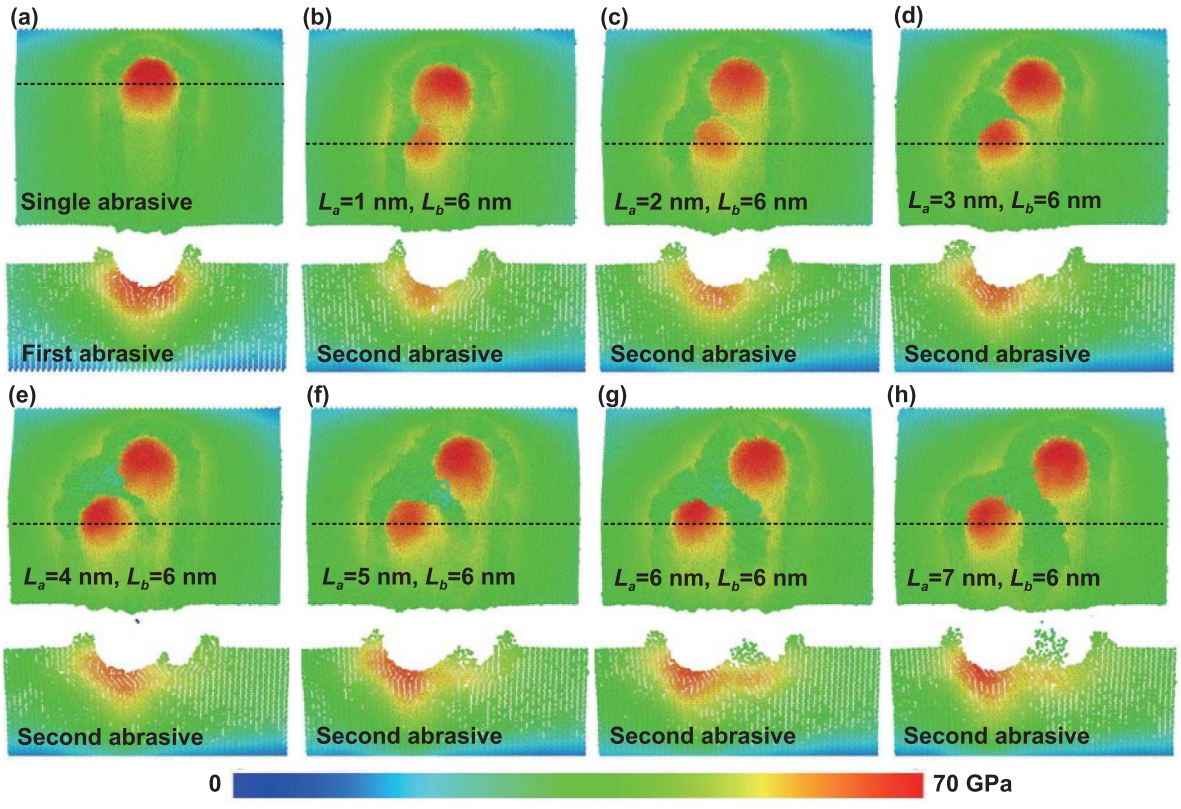

Figure 5. Stress distributions for different transverse interacted distances and a radial interacted distance of 6 nm. (a) Single-grit grinding, and (b)–(h) double-grit grinding with transverse interacted distances of 1 nm, 2 nm, 3 nm, 4 nm, 5 nm, 6 nm, and 7 nm, respectively.

removal during grinding. Figure 8 shows the bright field (BF) TEM images of damage behaviors of the ground subsurface. The diffraction spots shown in figure 8(d) indicate that the original GaN substrate is a perfect single crystal with a zone axis of [11–20]. Figure 8(a) indicates that the ductile subsurface does not contain cracks and brittle fractures, and a

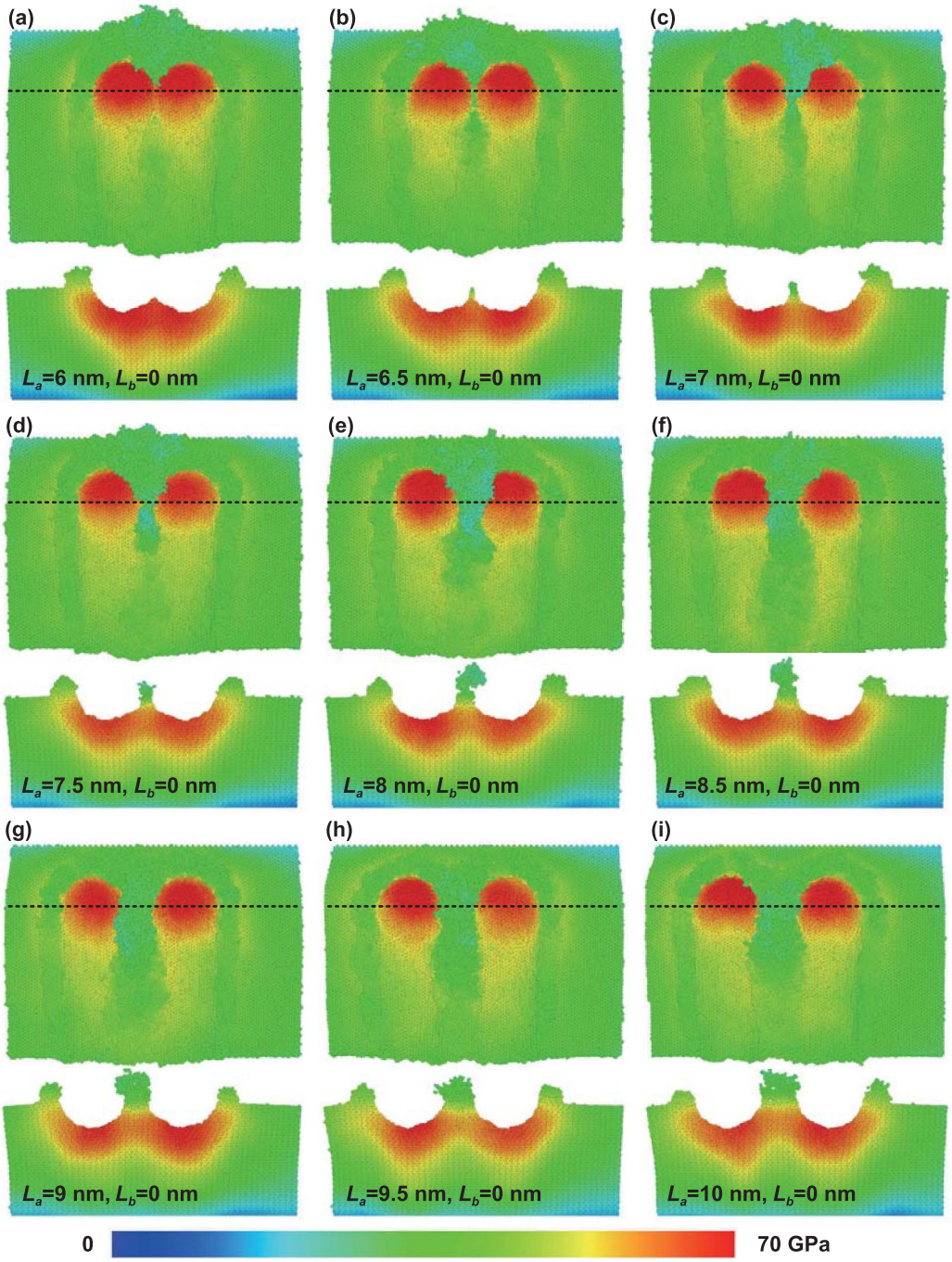

Figure 6. Stress distributions under different transverse interacted distances when the radial interacted distance is 0 nm. The transverse interacted distances of (a)–(i) are 6 nm, 6.5 nm, 7 nm, 7.5 nm, 8 nm, 8.5 nm, 9 nm, 9.5 nm and 10 nm, respectively.

plastic damage layer lies 200 nm beneath the ground surface. Figures 8(b) and (c) show that high-density stacking faults and dislocations are one of the main forms of plastic damage that occurs in GaN crystals during grinding. The main plastic deformation zone lies above the stacking fault and dislocation zones, which is similar to the subsurface damage induced by the quasi-static scratching [33]. To understand the essence of the main plastic deformation zone, more HR-TEM experiments need to be performed to characterize the main plastic deformation zone. The stacking faults generated under a high strain rate differ from those generated by low-strain-rate nanoscratching [33]. Only high-density stacking faults parallel to the (0001)-orientation plane are generated during the low strain-rate nanoscratch test. Figures 8(b) and (c) and (e) show that in addition to the stacking faults parallel to the (0001)-orientation plane, high-density stacking faults parallel to the {-1101} and {1-101} directions are generated during grinding. This phenomenon occurs because compared to

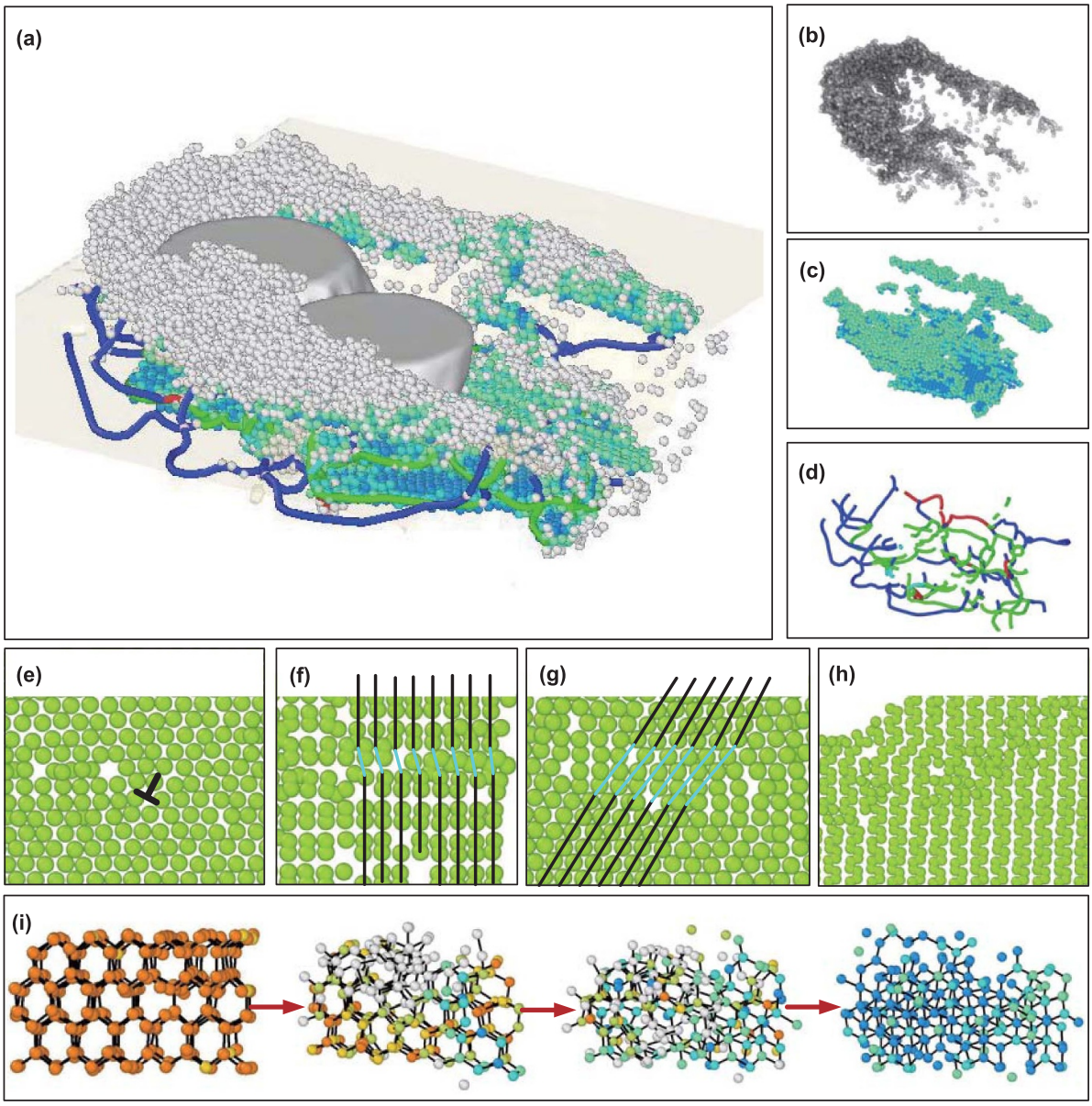

Figure 7. MD simulated results of subsurface damage mechanism of monocrystalline GaN induced by double-grits interacted grinding. (a) Overall damage morphology, (b) amorphous region (gray atoms), (c) cubic diamond atoms (green atoms), (d) and (e) dislocations (blue, orange, green, and purple lines), (f) and (g) stacking faults, (h) lattice distortions, and (i) phase transition path from hexagonal GaN (orange atoms) to cubic GaN (blue atoms). The radial and transverse interacted distances are 6 nm and 3 nm, respectively.

low-strain-rate nanoscratching, grinding generates a considerably higher strain rate, which induces a higher stress on the subsurface and activates crystal-plane slip along more crystal directions.

Figure 9 shows the HR-TEM images of the ground subsurface morphology. Figures 9(a) and (b) prove that surface amorphization is one of the main types of plastic damages in monocrystalline GaN induced by ultra-precision grinding, and figure 9(c) further confirms the existence of the high-density stacking faults. Similar to the simulated results, the surface atoms have relatively high energy and weak structural stability, producing an amorphization layer on the ground surface. The force exerted by the abrasives generates a shear stress along the close-packed plane that destroys the stacking sequence, generating stacking faults. As shown in figure 9(d), the interplanar spacings and included angles demonstrate that cubic GaN is generated by the high-pressure phase transition behavior. Figures 9(e) and (f) prove that dislocations and lattice distortions are also main forms of plastic damages induced in the grinding process. Lattice distortions increase the internal energy of materials and hinder dislocation slip. The TEM micrographs presented in figures 8 and 9 indicate that the forms of plastic damages from the ground surface to the subsurface are amorphous atoms, phase transition atoms, and a

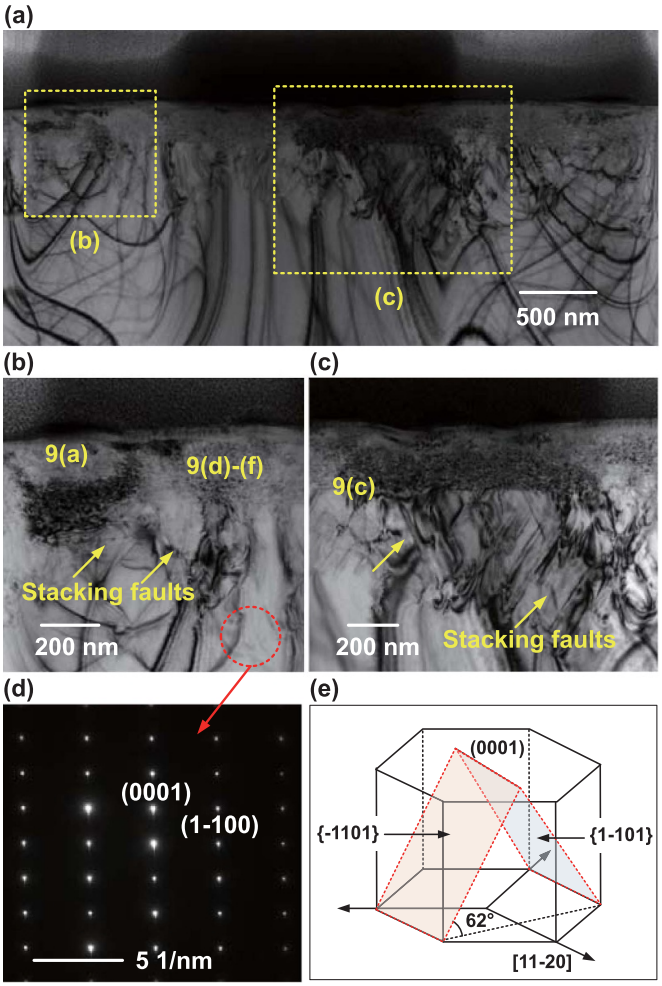

Figure 8. TEM results of subsurface damages. (a) Bright-field transmission electron microscopy (BF-TEM) images of the ground subsurface morphology, (b) and (c) enlarged images of (a), (d) diffraction spots of the monocrystalline GaN substrate, and (e) schematic diagram of stacking faults of the ground subsurface.

combination of dislocations and stacking faults. The aforementioned experimental results agree well with the MD results, which indicates that the simulated results are reliable.

The subsurface damage depth is one of the important indicators for evaluating the surface integrity during the ultra-precision machining of brittle materials [70, 71]. In this study, all the amorphous atoms, phase transition atoms, dislocations, stacking faults, and lattice distortions underneath the residual surface are regarded as subsurface damages. Therefore, the subsurface damage depth is defined as the distance from the residual surface to the deepest damage. Figure 10 presents the effect of the transverse interacted distance on the subsurface damage depth. Compared with the interacted distance in only one direction, the interacted distance in both radial and transverse directions achieved the shallower subsurface damage. When the radial interacted distance is 6 nm, the damage depth of the ground subsurface increases as the transverse interacted distance increases. The stress analysis in figure 5 demonstrates that increasing transverse interacted distance leads to an increase in the grinding stress of the second abrasive, resulting in an increase in the subsurface damage depth. However, there is no clear correlation between the transverse interacted distance and subsurface damage depth for the radial interacted distance of 0 nm.

Figure 11 shows the numbers of amorphous atoms under different interacted distances. As shown in figure 11(a), when the radial interacted distance is 6 nm, the number of amorphous atoms increases as the transverse interacted distance increases. This occurred because increasing transverse interacted distance can improve the material removal volume and grinding stress of the second abrasive, resulting in an increase in the number of amorphous atoms. As shown in figure 11(b), when the radial interacted distance is 0 nm, amorphous atoms increase and then decrease as the transverse interacted distance increases. When the transverse interacted distance is below 8 nm, as the transverse interacted distance increases, material removal volume and chip deformation increase, resulting in an increase in the number of amorphous atoms. However, when the transverse interacted distance is above than 8 nm, the grinding stress decreases as the transverse interacted distance increases, resulting in a decrease in the number of amorphous atoms.

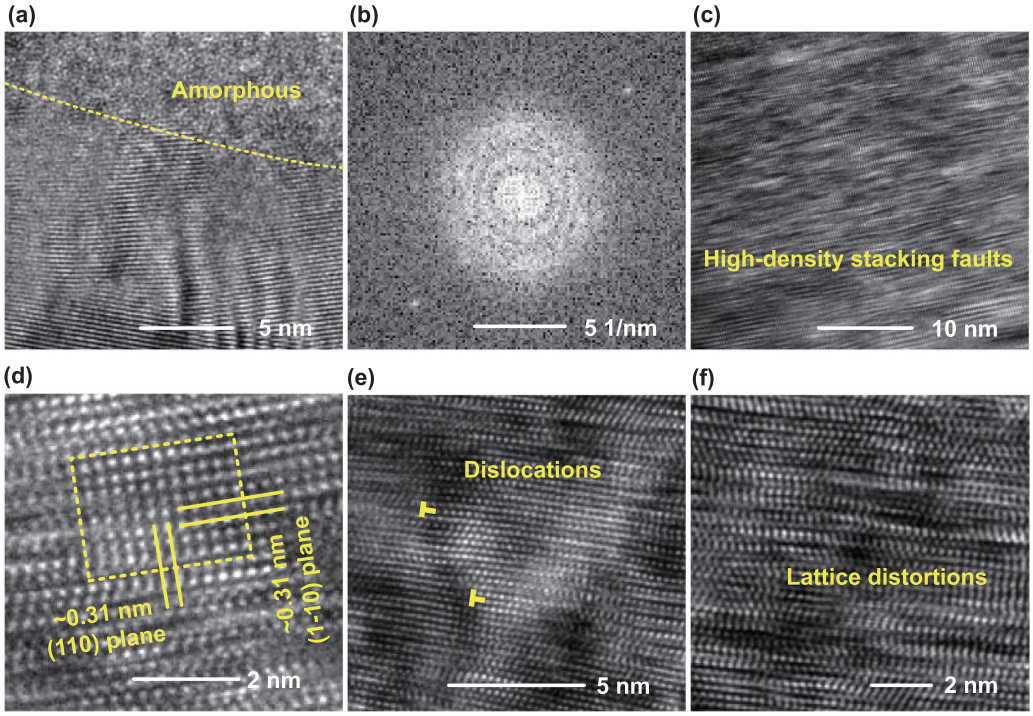

Figure 9. High-resolution transmission electron microscopy (HR-TEM) images of the ground subsurface morphology. (a) Amorphous and lattice distortions, (b) an amorphous halo ring in the Fourier transformation of (a), (c) high-density stacking faults, (d) cubic GaN generated during the high-pressure phase transition, (e) dislocations, and (f) lattice distortions.

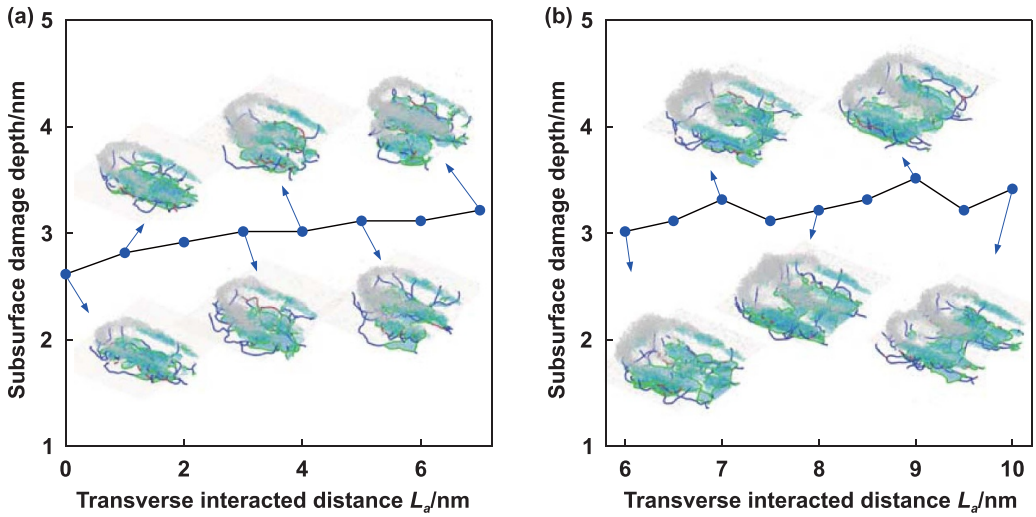

Figure 10. Influence of the transverse interacted distance on the subsurface damage depth. (a) The radial interacted distance is 6 nm, and (b) the radial interacted distance is 0 nm. The inset images are surface and subsurface damages under different interacted distances, including amorphous atoms (gray atoms), cubic diamond phases (gray atoms) and dislocations (blue, orange, green, and purple lines).

Figures 12 and 13 show the numbers of phase transition atoms of cubic GaN and dislocation lengths under different interacted distances, respectively. It can be found that there is no clear correlation between the transverse interacted distance and number of atoms in the phase transition and dislocation length. This occurred because the high-pressure phase transition and dislocation length are determined by the stress and material removal volume. For a constant radial interacted distance and increasing transverse interacted distance, the stress decreases and then gradually stabilizes, whereas the material removal volume increases and then stabilizes. Therefore, transverse interacted distance is not monotonically related to the number of atoms in the phase transition and dislocation length.

3.4. Abrasive damage

Figure 14 shows that the amorphization transition is the main form of damage behaviors in abrasive wear, such that the proportion of abrasive amorphization can be used as a measure

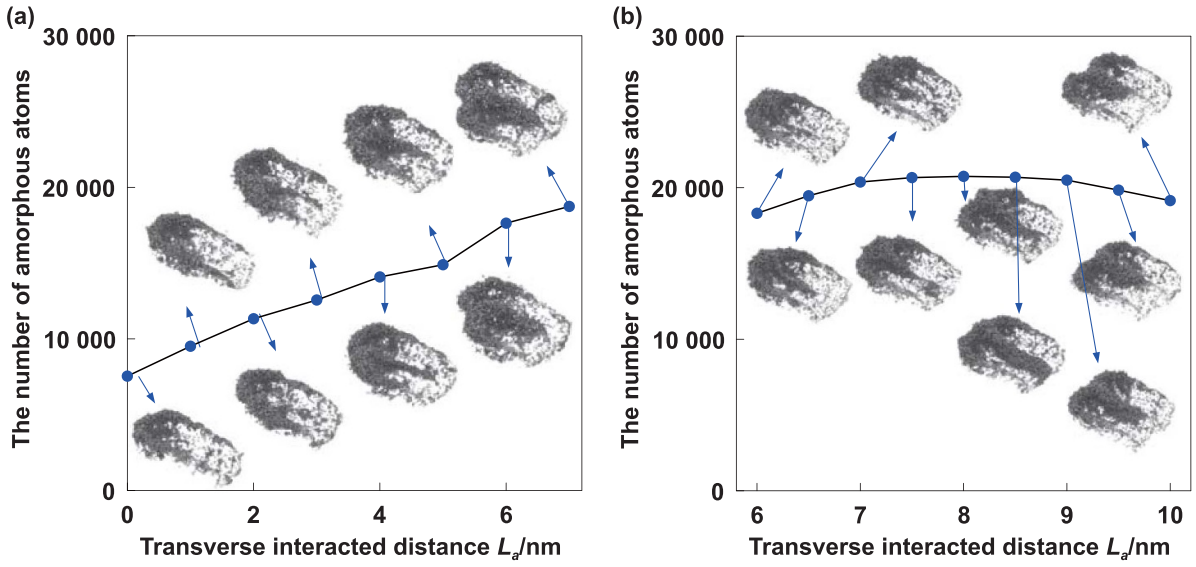

Figure 11. Influence of the transverse interacted distance on the number of amorphous atoms. (a) The radial interacted distance is 6 nm, and (b) the radial interacted distance is 0 nm.

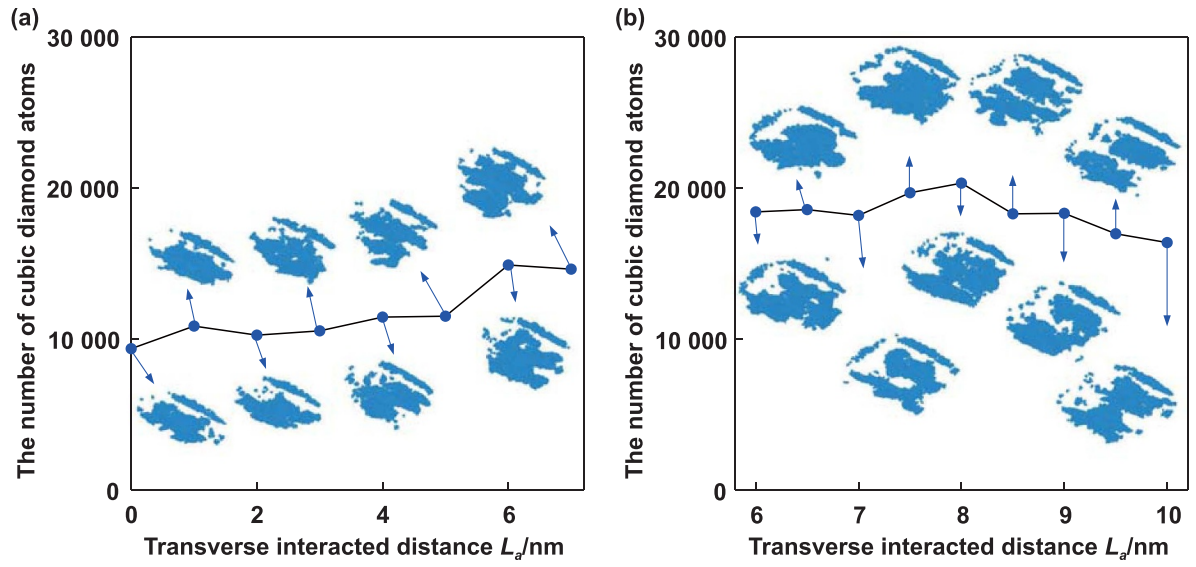

Figure 12. Influence of the transverse interacted distance on the number of cubic diamond atoms. (a) The radial interacted distance is 6 nm, and (b) the radial interacted distance is 0 nm.

of the damage degree of the abrasives [72, 73]. The morphologies of the abrasives after grinding show more severe amorphization damage at the flank face than that at the rake face. The high elastic recovery rate of the residual GaN material under a high contact stress during grinding [74, 75] makes the flank face prone to friction after grinding than the rake face, resulting in severe wear of the flank face. As shown in figure 14(a), when the radial interacted distance is 6 nm, the amorphization proportion of the first abrasive is larger than that of the second abrasive for the same scratch lengths. As the transverse interacted distance increases, the amorphization proportion gradually increases and then stabilizes. This result is obtained because the elimination of coupling to the first abrasive reduces the volume of material removed by the second abrasive and the elastic recovery depth of the residual materials, effectively reducing the contact stress and flank wear induced by the elastic recovery of the residual materials. The stress generated by the second abrasive also suppresses the elastic recovery of the residual materials of the first abrasive, reducing the flank wear of the first abrasive compared to that of single-grit grinding. As shown in figure 14(b), when the radial interacted distance is 0 nm, there is no clear correlation between the transverse interacted distance and amorphization proportion of abrasive atoms, and the amorphization proportion of the first abrasive is close to that of the second abrasive.

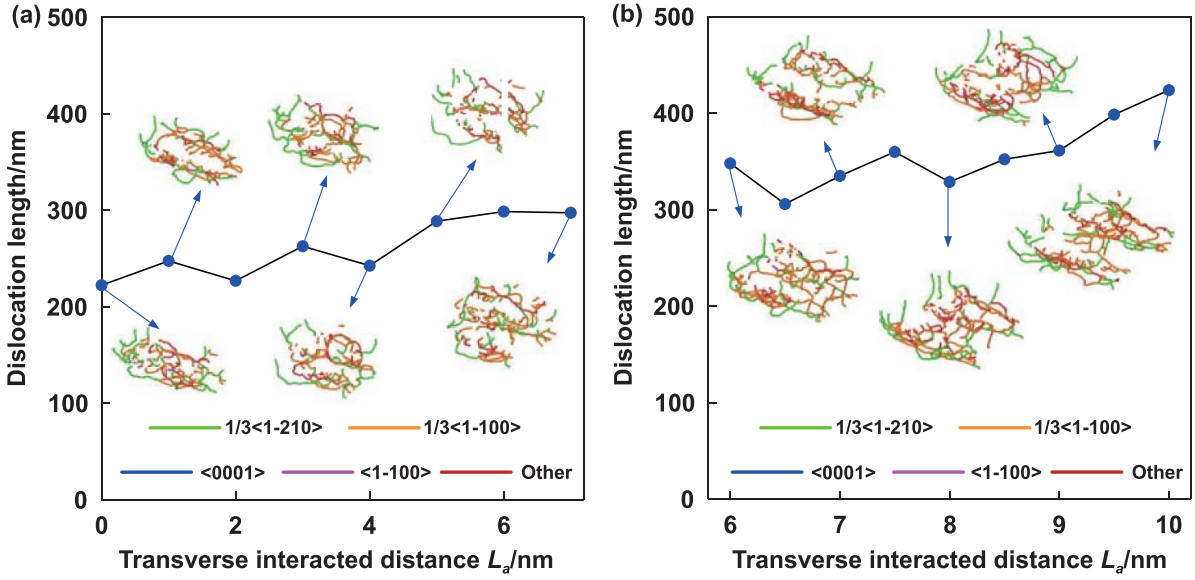

Figure 13. Influence of the transverse interacted distance on the dislocation length. (a) The radial interacted distance is 6 nm, and (b) the radial interacted distance is 0 nm. The inset images show dislocation loops with different directions. The blue, green, orange, and purple dislocation loops have 1/3<1–210>, <1–100>, 1/3<1–100>, and other crystal orientations, respectively.

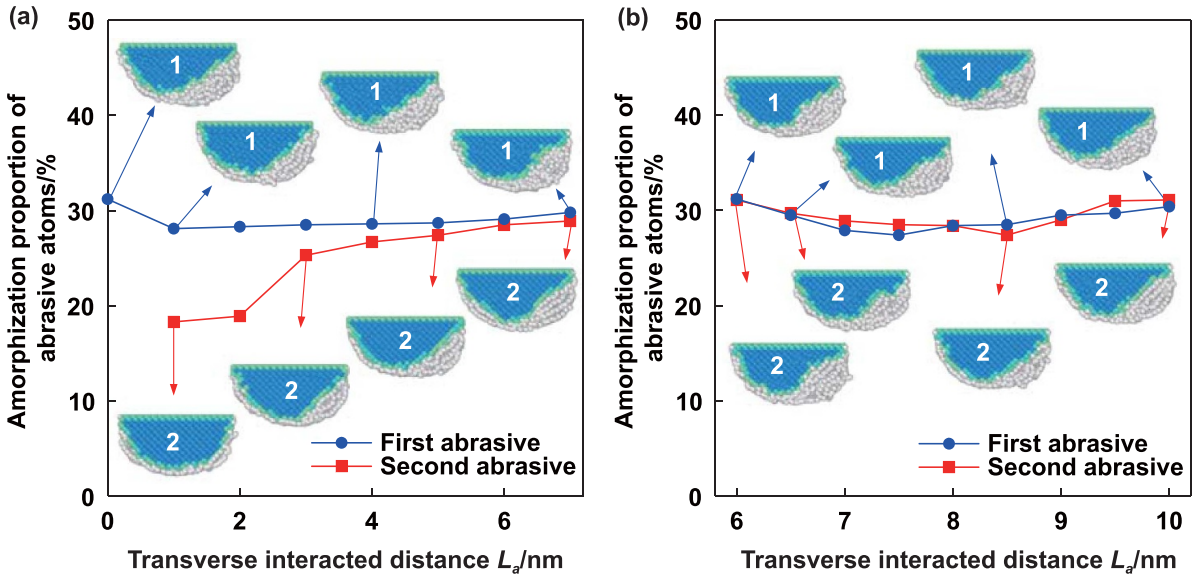

Figure 14. Amorphization proportion of abrasive atoms under different interacted distances (scratch lengths of all abrasives are 10 nm). (a) The radial interacted distance is 6 nm, and (b) the radial interacted distance is 0 nm. Inset images show the abrasive morphologies after grinding, where the blue and gray atoms represent cubic and amorphous diamond atoms, respectively.

4. Conclusions

The effect of coupling between abrasives on damage accumulation and material removal during grinding of GaN crystals was investigated by conducting MD simulations of interactive double-grit grinding of monocrystalline GaN. The simulated grinding force, coefficient of friction, stress distribution, plastic damage behavior, and abrasive damage were analyzed. The following conclusions were drawn from the study.

- The results of grinding tests combined with cross-sectional TEM micrographs validate the simulated plastic damage behaviors, i.e. the amorphization transition, the high-pressure phase transition, stacking faults, dislocation slips, and lattice distortions. For nonzero interaction distances in both the radial and transverse directions, the damage depth of the ground subsurface increases as the transverse interacted distance increases. There is no clear correlation between the transverse interacted distance and number of atoms in the phase transition and the dislocation length.

- For nonzero distances in both the radial and transverse directions, eliminating the coupling action between the two abrasives results in the second abrasive exerting a smaller grinding force and stress than the first abrasive; as the transverse interacted distance increases, the grinding force and stress increase and then stabilize. Only the transverse interacted distance is nonzero, the stress on the subsurface gradually decreases as the transverse interacted distance increases.
- For nonzero interaction distances in both the radial and transverse directions, elimination of the coupling action between abrasives and the number of atoms that have accumulated in front of the abrasives causes the coefficient of friction to decrease and then increase as the transverse interacted distance increases.
- The amorphization transition is the main form of damage incurred during abrasive wear. Amorphization damage is more severe at the flank face than that at the rake face because of the high elastic recovery of the residual material under a high contact stress. For nonzero interaction distances in both the radial and transverse directions, the amorphization proportion of the first abrasive is smaller than that of the second abrasive for the same scratch lengths. As the transverse interacted distance increases, the amorphization proportion of the second abrasive gradually increases and stabilizes because of the elimination of coupling to the first abrasive.
- Only the transverse interacted distance is nonzero, there is no clear correlation between the transverse interacted distance and the grinding force, coefficient of friction, subsurface damage depth, number of atoms in the phase transition, dislocation length, and abrasive damage.

Acknowledgments

This work was supported by the National Natural Science Foundation of China (52375420, 52005134 and 51675453), Natural Science Foundation of Heilongjiang Province of China (YQ2023E014), Self-Planned Task (No. SKLRS202214B) of State Key Laboratory of Robotics and System (HIT), China Postdoctoral Science Foundation (2022T150163), Young Elite Scientists Sponsorship Program by CAST (No. YESS20220463), State Key Laboratory of Robotics and System (HIT) (SKLRS-2022-ZM-14), Open Fund of Key Laboratory of Microsystems and Microstructures Manufacturing (HIT) (2022KM004), and Fundamental Research Funds for the Central Universities (Grant Nos. HIT.OCEF.2022024 and FRFCU5710051122).

Author statement

This work 'Damage evolution and removal behaviors of GaN crystals involved in double-grits grinding' was original research that has not been published, and not under consideration for publication elsewhere, in whole or in part.

ORCID iDs

Chen Li https://orcid.org/0000-0002-8259-0731
Yunfeng Peng https://orcid.org/0000-0002-8917-508X
Yanquan Geng https://orcid.org/0000-0003-3499-0551

References

[1] Goldberger J, He R R, Zhang Y F, Lee S, Yan H Q, Choi H J and Yang P D 2003 Single-crystal gallium nitride nanotubes *Nature* **422** 599–602
[2] Wheeler J M, Niederberger C, Tessarek C, Christiansen S and Michler J 2013 Extraction of plasticity parameters of GaN with high temperature, *in situ* micro-compression *Int. J. Plast.* **40** 140–51
[3] Ganchenkova M G and Nieminen R M 2006 Nitrogen vacancies as major point defects in gallium nitride *Phys. Rev. Lett.* **96** 196402
[4] Li C, Li X L, Wu Y Q, Zhang F H and Huang H 2019 Deformation mechanism and force modelling of the grinding of YAG single crystals *Int. J. Mach. Tools Manuf.* **143** 23–37
[5] Yan J W, Lu J B, Huang Y L, Pan J S and Yan Q S 2022 Fenton reaction chemical mechanical polishing liquid composition optimization of polishing GaN wafer *Diam. Abrasives Eng.* **42** 610–6
[6] Li C, Wu Y Q, Li X L, Ma L J, Zhang F H and Huang H 2020 Deformation characteristics and surface generation modelling of crack-free grinding of GGG single crystals *J. Mater. Process. Technol.* **279** 116577
[7] Kubota A and Iwakiri A 2019 Tribochemical polishing of bulk gallium nitride substrate *Precis. Eng.* **56** 69–79
[8] Pan J S, Wu Y S, Zhuo Z J, Wang H, Zheng Q B and Yan Q S 2023 Experimental study of single-crystal GaN wafer electro-Fenton magnetorheological complex friction wear *Tribol. Int.* **180** 108260
[9] Pan J S, Zhuo Z J, Zhang Q X, Zheng Q B and Yan Q S 2022 Friction and wear mechanisms for single crystal GaN based on an electro-Fenton enhanced chemical reaction *Wear* **498–499** 204315
[10] Shi D, Zhou W and Zhao T C 2023 Polishing of diamond, SiC, GaN based on the oxidation modification of hydroxyl radical: status, challenges and strategies *Mater. Sci. Semicond. Process.* **166** 107737
[11] Zhang L F, Wu B, Zhang Y and Deng H 2023 Highly efficient and atomic scale polishing of GaN via plasma-based atom-selective etching *Appl. Surf. Sci.* **620** 156786
[12] Zhang L F, Lu D and Deng H 2022 Study on material removal mechanisms in electrochemical etching-enhanced polishing of GaN *J. Manuf. Process.* **73** 903–13
[13] Aida H, Takeda H, Kim S W, Aota N, Koyama K, Yamazaki T and Doi T 2014 Evaluation of subsurface damage in GaN substrate induced by mechanical polishing with diamond abrasives *Appl. Surf. Sci.* **292** 531–6
[14] Gong H, Pan G S, Zhou Y, Shi X L, Zou C L and Zhang S M 2015 Investigation on the surface characterization of Ga-faced GaN after chemical-mechanical polishing *Appl. Surf. Sci.* **338** 85–91
[15] Yu X, Zhang B G, Wang R, Kao Z, Yang S H and Wei W 2021 Effect of photocatalysts on electrochemical properties and chemical mechanical polishing rate of GaN *Mater. Sci. Semicond. Process.* **121** 105387

[16] Zhang L F and Deng H 2020 Highly efficient and damage-free polishing of GaN (0 0 0 1) by electrochemical etching-enhanced CMP process *Appl. Surf. Sci.* **514** 145957
[17] Huang H, Li X L, Mu D K and Lawn B R 2021 Science and art of ductile grinding of brittle solids *Int. J. Mach. Tools Manuf.* **161** 103675
[18] Zheng Z D, Huang K, Lin C T, Zhang J G, Wang K, Sun P and Xu J F 2022 An analytical force and energy model for ductile-brittle transition in ultra-precision grinding of brittle materials *Int. J. Mech. Sci.* **220** 107107
[19] Li C, Li X L, Huang S Q, Li L Q and Zhang F H 2021 Ultra-precision grinding of $Gd_3Ga_5O_{12}$ crystals with graphene oxide coolant: material deformation mechanism and performance evaluation *J. Manuf. Process.* **61** 417–27
[20] Piao Y C, Li C, Hu Y X, Cui H L, Luo X C, Geng Y Q and Zhang F H 2024 Nanoindentation induced anisotropy of deformation and damage behaviors of MgF_2 crystals *J. Mater. Res. Technol.* **28** 4615–25
[21] Zhang Y, Wu T, Li C, Wang Y F, Geng Y Q and Dong G J 2022 Numerical simulations of grinding force and surface morphology during precision grinding of leucite glass ceramics *Int. J. Mech. Sci.* **231** 107562
[22] Huang W H and Yan J W 2023 Effect of tool geometry on ultraprecision machining of soft-brittle materials: a comprehensive review *Int. J. Extrem Manuf.* **5** 012003
[23] Shamray S, Azarhoushang B, Paknejad M and Buechler A 2022 Ductile-brittle transition mechanisms in micro-grinding of silicon nitride *Ceram. Int.* **48** 34987–98
[24] Yang M J, Liu C, Guo B J, Liu K, Tu R, Ohmori H and Zhang S 2023 Understanding of highly-oriented 3C-SiC ductile-brittle transition mechanism in ELID ultra-precision grinding *Mater. Charact.* **203** 113136
[25] Wang S, Sun G Y, Zhao Q L and Yang X D 2023 Monitoring of ductile–brittle transition mechanisms in sapphire ultra-precision grinding used small grit size grinding wheel through force and acoustic emission signals *Measurement* **210** 112557
[26] Li C, Zhang F H, Meng B B, Rao X S and Zhou Y 2017 Research of material removal and deformation mechanism for single crystal GGG ($Gd_3Ga_5O_{12}$) based on varied-depth nanoscratch testing *Mater Des* **125** 180–8
[27] Li C, Piao Y C, Zhang F H, Zhang Y, Hu Y X and Wang Y F 2023 Understand anisotropy dependence of damage evolution and material removal during nanoscratch of MgF_2 single crystals *Int. J. Extrem. Manuf.* **5** 015101
[28] Zhang Z Q, Shi K N, Huang X C, Shi Y Y, Zhao T, He Z and Song Y H 2022 Development of a probabilistic algorithm of surface residual materials on Si_3N_4 ceramics under longitudinal torsional ultrasonic grinding *Ceram. Int.* **48** 12028–37
[29] Qu S S, Yao P, Gong Y D, Chu D K, Yang Y Y, Li C W, Wang Z L, Zhang X P and Hou Y 2022 Environmentally friendly grinding of C/SiCs using carbon nanofluid minimum quantity lubrication technology *J. Clean. Prod.* **366** 132898
[30] Tao H F, Liu Y H, Zhao D W and Lu X C 2023 Ductile deformation and subsurface damage evolution mechanism of silicon wafer induced by ultra-precision grinding process *Tribol. Int.* **189** 108879
[31] Li M, Guo X G, Dai S Y, Yuan S, Ma J L, Liu F M, Zhang L M, Guo D M and Zhou P 2022 Effect of grinding damage on cutting force and ductile machining during single grain scratching of monocrystalline silicon *Mater. Sci. Semicond. Process.* **151** 107019
[32] Wang Y Q, Li X L, Wu Y Q, Mu D K and Huang H 2021 The removal mechanism and force modelling of gallium oxide single crystal in single grit grinding and nanoscratching *Int. J. Mech. Sci.* **204** 106562
[33] Li C, Piao Y, Meng B B, Zhang Y, Li L Q and Zhang F H 2022 Anisotropy dependence of material removal and deformation mechanisms during nanoscratch of gallium nitride single crystals on (0001) plane *Appl. Surf. Sci.* **578** 152028
[34] Li C, Piao Y, Meng B B, Hu Y X, Li L Q and Zhang F H 2022 Phase transition and plastic deformation mechanisms induced by self-rotating grinding of GaN single crystals *Int. J. Mach. Tools Manuf.* **172** 103827
[35] Tan S P, Wang Y P, Huang H, Wu Y Q and Huang H 2022 Deformation and removal mechanism of single crystal gallium nitride in nanoscratching *Ceram. Int.* **48** 23793–9
[36] Guo M X, Tao J B, Wu C J, Luo C and Lin Z J 2023 High-speed grinding fracture mechanism of C_f/SiC composite considering interfacial strength and anisotropy *Ceram. Int.* **49** 2600–12
[37] Li C, Zhang F H, Meng B B, Liu L F and Rao X S 2017 Material removal mechanism and grinding force modelling of ultrasonic vibration assisted grinding for SiC ceramics *Ceram. Int.* **43** 2981–93
[38] Lou Z Z, Yan Y D, Wang J Q, Zhang A X, Cui H L, Li C and Geng Y Q 2024 Exploring the structural color of micro-nano composite gratings with FDTD simulation and experimental validation *Opt. Express* **32** 2432–51
[39] Li C, Hu Y X, Huang S Q, Meng B B, Piao Y and Zhang F H 2022 Theoretical model of warping deformation during self-rotating grinding of YAG wafers *Ceram. Int.* **48** 4637–48
[40] Huang S Q, Gao S, Huang C Z and Huang H 2022 Nanoscale removal mechanisms in abrasive machining of brittle solids *Diam. Abrasives Eng.* **42** 257–67
[41] Li C, Zhang F H, Wang X and Rao X S 2018 Repeated nanoscratch and double nanoscratch tests of Lu_2O_3 transparent ceramics: material removal and deformation mechanism, and theoretical model of penetration depth *J. Eur. Ceram. Soc.* **38** 705–18
[42] Meng B B, Yuan D D and Xu S L 2019 Coupling effect on the removal mechanism and surface/subsurface characteristics of SiC during grinding process at the nanoscale *Ceram. Int.* **45** 2483–91
[43] Guo X G, Li Q, Liu T, Zhai C H, Kang R K and Jin Z J 2016 Molecular dynamics study on the thickness of damage layer in multiple grinding of monocrystalline silicon *Mater. Sci. Semicond. Process.* **51** 15–19
[44] Zhou P, Zhu N N, Xu C Y, Niu F L, Li J and Zhu Y W 2021 Mechanical removal of SiC by multi-abrasive particles in fixed abrasive polishing using molecular dynamics simulation *Comput. Mater. Sci* **191** 110311
[45] Zhao P Y, Zhao B, Pan J S and Wu J W 2022 Superimpose mechanism of surface generation process in grinding of monocrystalline silicon using molecular dynamics simulation *Mater. Sci. Semicond. Process.* **147** 106684
[46] Hu Z W, Chen Y, Lai Z Y, Yu Y Q, Xu X P, Peng Q and Zhang L 2022 Coupling of double grains enforces the grinding process in vibration-assisted scratch: insights from molecular dynamics *J. Mater. Process. Technol.* **304** 117551
[47] Karkalos N E and Markopoulos A P 2020 Molecular dynamics study of the effect of abrasive grains orientation and spacing during nanogrinding *Micromachines* **11** 712
[48] Dai H F, Yue H X, Hu Y and Li P 2021 The removal mechanism of monocrystalline Si in the process of double diamond abrasive polishing by molecular dynamics simulation *Tribol. Lett.* **69** 66
[49] Li C, Hu Y X, Zhang F H, Geng Y Q and Meng B B 2023 Molecular dynamics simulation of laser assisted grinding of GaN crystals *Int. J. Mech. Sci.* **239** 107856
[50] Dai H F, Hu Y, Wu W L, Yue H X, Meng X S, Li P and Duan H G 2021 Molecular dynamics simulation of

ultra-precision machining 3C-SiC assisted by ion implantation *J. Manuf. Process.* **69** 398–411
[51] Wang J Q, Yan Y D, Li C and Geng Y Q 2023 Material removal mechanism and subsurface characteristics of silicon 3D nanomilling *Int. J. Mech. Sci.* **242** 108020
[52] Gao S, Wang H X, Huang H and Kang R K 2023 Molecular simulation of the plastic deformation and crack formation in single grit grinding of 4H-SiC single crystal *Int. J. Mech. Sci.* **247** 108147
[53] Chen M H and Dai H F 2022 Molecular dynamics study on grinding mechanism of polycrystalline silicon carbide *Diam. Relat. Mater.* **130** 109541
[54] Huang Y H, Zhou Y Q, Li J M and Zhu F L 2023 Understanding of the effect of wear particles removal from the surface on grinding silicon carbide by molecular dynamics simulations *Diam. Relat. Mater.* **137** 110150
[55] Wu Y L, Tan J, Li X M, Qiu Z J and Zhang R Z 2023 Molecular dynamics study on friction of high-entropy alloy FeNiCrCoCu *Mater. Today Commun.* **37** 107107
[56] Huang Y H, Wang M C, Xu Y X and Zhu F L 2020 Investigation on gallium nitride with N-vacancy defect nano-grinding by molecular dynamics *J. Manuf. Process.* **57** 153–62
[57] Zhang C Y, Dong Z G, Yuan S, Guo X G, Kang R K and Guo D M 2021 Study on subsurface damage mechanism of gallium nitride in nano-grinding *Mater. Sci. Semicond. Process.* **128** 105760
[58] Li L and Ge P Q 2021 Analysis of SPH and FEM coupling simulation of abrasive grain scratching single crystal SiC *Surf. Technol.* **50** 44–53
[59] Jiang Q Q, Zhang L and Yang C F 2021 An analytical model for estimation of the stress field and cracks caused by scratching anisotropic single crystal gallium nitride *Mater. Sci. Semicond. Process.* **122** 105446
[60] Luo X C, Goel S and Reuben R L 2012 A quantitative assessment of nanometric machinability of major polytypes of single crystal silicon carbide *J. Eur. Ceram. Soc.* **32** 3423–34
[61] Goel S, Luo X C and Reuben R L 2012 Shear instability of nanocrystalline silicon carbide during nanometric cutting *Appl. Phys. Lett.* **100** 231902
[62] Nord J, Albe K, Erhart P and Nordlund K 2003 Modelling of compound semiconductors: analytical bond-order potential for gallium, nitrogen and gallium nitride *J. Phys.: Condens. Matter* **15** 5649–62
[63] Los J H and Fasolino A 2003 Intrinsic long-range bond-order potential for carbon: performance in Monte Carlo simulations of graphitization *Phys. Rev.* B **68** 024107
[64] Hou X, Li J Y, Li Y Z and Tian Y 2022 Intermolecular and surface forces in atomic-scale manufacturing *Int. J. Extrem. Manuf.* **4** 022002
[65] Wu L, Yu B, Zhang P, Feng C, Chen P, Deng L, Gao J, Chen S, Jiang S and Qian L 2020 Rapid identification of ultrathin amorphous damage on monocrystalline silicon surface *Phys. Chem. Chem. Phys.* **22** 12987–95
[66] Zhang Y F, Zhu S L, Zhao Y Y and Yin Y H 2022 A material point method based investigation on crack classification and transformation induced by grit geometry during scratching silicon carbide *Int. J. Mach. Tools Manuf.* **177** 103884
[67] Jiang Q Q, Zhang L and Yang C F 2022 Analysis of crack initiation load and stress field in double scratching of single crystal gallium nitride *Eng. Fract. Mech.* **274** 108732
[68] Zhao L, Zhang J G, Zhang J J, Hartmaier A and Sun T 2022 Formation of high density stacking faults in polycrystalline 3C-SiC by vibration-assisted diamond cutting *J. Eur. Ceram. Soc.* **42** 5448–57
[69] Zhang Y C, Song R B, Wang Y J, Cai C H, Wang H B and Wang K K 2023 The excellent strength and ductility matching of directly warm-rolled V-alloyed medium manganese steel by stacking fault networks *Mater. Des.* **227** 111719
[70] Meng B B and Li C 2023 Effect of anisotropy on deformation and crack formation under the brittle removal of 6H-SiC during SPDT process *J. Adv. Res.* (https://doi.org/10.1016/j.jare.2023.04.004)
[71] Zhang Y, Wang Q, Li C, Piao Y, Hou N and Hu K N 2022 Characterization of surface and subsurface defects induced by abrasive machining of optical crystals using grazing incidence x-ray diffraction and molecular dynamics *J. Adv. Res.* **36** 51–61
[72] Qiang B Y, Shi K N, Liu N, Ren J X and Shi Y Y 2023 Integrating physics-informed recurrent Gaussian process regression into instance transfer for predicting tool wear in milling process *J. Manuf. Syst.* **68** 42–55
[73] Wang S, Dong H, Gu Y, Wang M and Wang J W 2022 Research on grinding quality and removal mechanism of polycrystalline diamond tools *Diam. Abrasives Eng.* **42** 467–72
[74] Kataoka R and Shamoto E 2019 Influence of vibration in cutting on tool flank wear: fundamental study by conducting a cutting experiment with forced vibration in the depth-of-cut direction *Precis. Eng.* **55** 322–9
[75] Pálmai Z 2013 Proposal for a new theoretical model of the cutting tool's flank wear *Wear* **303** 437–45